BIBECHANA
Vol. 21, No. 3, December 2024, 254-261

ISSN 2091-0762 (Print), 2382-5340 (Online)
Journal homepage: http://nepjol.info/index.php/BIBECHANA
Publisher: Dept. of Phys., Mahendra Morang A. M. Campus (Tribhuvan University) Biratnagar

Composition optimization of Ni-Zn ferrites for magnetic hyperthermia: structural, morphological and spectroscopic study

D. Parajuli[1,2,*], P. V. Ramana[3], N. Murali[4], S. Bista[5], M. Sharma[5], K. Samatha[6]

[1] *Research Center for Applied Science and Technology, Tribhuvan University, Kathmandu -44613, Kirtipur, Nepal*
[2] *Tri-Chandra Multiple Campus, Ghantaghar, Kathmandu-44600, Nepal*
[3] *Sri DNR Government Degree College for Women Palakol-534260, West Godavari, Andhra Pradesh, India*
[4] *Department of Engineering Physics, AUCE, Andhra University, Visakhapatnam-530003, India*
[5] *College of Biomedical Engineering and Medical Science, Purbanchal University, Kupondole, Lalitpur, 44600, Nepal*
[6] *Department of Physics, Andhra University, Visakhapatnam-530003, India*

[*]Corresponding author: Email: deepenparaj@gmail.com

Abstract

The optimization of the appropriate composition is necessary for the characteristics suitable for magnetic hyperthermia by varying the amount of iron in the ferrite composition. The NiZn ferrite with the composition $Ni_{0.65}Zn_{0.35}Fe_2O_4$, $Ni_{0.65}Zn_{0.40}Fe_{1.95}O_4$, *and* $Ni_{0.60}Zn_{0.35}Fe_{2.05}O_4$ *indicated by IN, IE, and ID respectively were synthesized from sol-gel approach. XRD shows cubic spinel structure except for one extra peak in all three samples (IN 800℃; IE 800℃, and ID 900℃; 800℃, 900℃ and 1000℃) around 2= 40.9° is related to the iron oxide (Fe2O3) and is related to JCPDS 89-8104). The formation of the additional peak is due to the diffusion of atoms in the heating process. The variations in crystallite size and particle size are due to iron content. Their effect on magnetic properties and hence in hyperthermia are under study.*

Keywords
Ni-Zn Ferrites, SEM-EDX, FTIR, Hyperthermia.

Article information
Manuscript received: May 7, 2024; Revised: June 20, 2024; Accepted: June 23, 2024
DOI https://doi.org/10.3126/bibechana.v21i3.65529

1 Introduction

Hyperthermia, the application of heat to treat disease, has ancient roots dating back to Egyptian, Indian, and Chinese civilizations. The therapeutic use of heat was historically limited to treating infections, improving circulation, and easing muscle pain. However, its scientific exploration began in earnest in the 19th and 20th centuries. In 1866, German surgeon Carl Busch reported using heat to treat tumors, and in the 20th century, advancements in technology facilitated more precise applications of hyperthermia [1]. This is highly applicable in medical applications: 1) Cancer Treatment, 2) Enhanced Drug Delivery, 3) Immune Response Stimulation, 4) Pain management etc. In cancer treatment, there are three hyperthermia: Local Hyperthermia (Targets small areas, typically tumors, using external devices like microwave, ultrasound, or radiofrequency to raise tissue temperature.), Regional Hyperthermia (treats larger areas of the body, such as limbs or organs, often in combination with other treatments like chemotherapy.) and Whole-body Hyperthermia (used for metastatic cancer, raising the body's core temperature to enhance the effects of other cancer treatments.) [1] In enhanced drug delivery, hyperthermia increases cell membrane permeability, facilitating the uptake of chemotherapeutic drugs. It can enhance the efficacy of drug-loaded nanoparticles and liposomes, targeting tumor sites more effectively. In immune response stimulation, heat can stimulate immune responses by increasing the expression of heat shock proteins, which help the immune system recognize and attack cancer cells. In pain management, it is used in physiotherapy to relieve muscle and joint pain, leveraging its ability to improve blood flow and reduce muscle stiffness [1]. Recent research focuses on magnetic nanoparticles that can be heated in an alternating magnetic field, providing targeted hyperthermia with minimal damage to surrounding tissues [**?**]. Integrating hyperthermia with radiation and immunotherapy has shown promising results, enhancing treatment efficacy and reducing side effects. Advances in imaging and thermal dosimetry have improved hyperthermia's precision, allowing for real-time non-invasive treatment monitoring and adjustments [2].

The extensive research conducted on the Ni-Zn ferrite system [3–6] has demonstrated that Ni-Zn bulk ferrite emerges as the optimal core material for high-frequency applications. This is due to its advantageous properties, such as high saturation magnetization, elevated Curie temperature, favorable magnetic permeability, low power loss, and high DC resistivity [7, 8]. Transforming bulk Ni-Zn ferrite into nanostructures offers significant potential for enhancing specific properties like saturation magnetization, initial permeability, particle size, and DC resistivity. Consequently, this material holds promise for various applications, including magnetic data storage, targeted drug delivery systems, MRI contrast enhancement, and serving as a heating agent in magnetic fluid hyperthermia [9, 10]. Achieving desired variations in multiple parameters tailored for each application requires meticulous control over the synthesis process to produce the material in nano form.

It is known that tailoring the chemical composition allows control of magnetic properties [11–13]. These properties depend primarily on the exchange interactions, which depend upon the types and concentrations of different cations present in the composition [14, 15]. Numerous researchers have made efforts [16–18] to obtain the least-sized particles with superior magnetic properties in nano Ni1-xZnxFe2O4 ferrites by choosing an appropriate zinc concentration (x). On the other hand, research has revealed that studies involving varied iron content in bulk or nano Ni-Zn ferrites are severely inadequate [19–21].

In any ferrite system, the arrangement of substituted ions within the structure plays a crucial role in altering the electromagnetic properties [22]. To develop a suitable material with desired characteristics, it's essential to thoroughly comprehend how different cations occupy positions within the A and B sub-lattices [23]. For instance, achieving magnetic hyperthermia necessitates materials exhibiting high saturation magnetization, low coercivity, and a significant Curie temperature [24]. Enhancing processing conditions and focusing on consequent magnetic properties can lead to the fabrication of superior materials for magnetic hyperthermia applications [25].

The study undertakes a methodical examination aimed at obtaining a nano ferrite composition. It aims to significantly enhance specific saturation magnetization through a comprehensive understanding of how cation distribution varies with different levels of iron content in the ferrite composition. Here, we present and analyze their structural, morphological, and spectroscopic data.

2 Method of preparation

The sol-gel process was adopted in preparing the Ni-Zn nanoferrites with varying amounts of iron in the composition. The nitrates of nickel, zinc, and iron are mixed in stoichiometric proportion along with deionized water and stirred for 2 hrs and then mixed with a chelating agent polyethylene glycol (PEG) (10g of PEG mixed in 100mL deionized water) in 1:1 ratio and dehydrated at 100°C. The involved reactions are:

(a) $0.65\ Ni(NO_3)_2.6H_2O + 0.35\ Zn$

$(NO_3)_2.6H_2O + 2\ Fe\ (NO_3)_3.9H_2O + PEG \rightarrow Ni_{0.65}Zn_{0.35}Fe_2O_4 + 8NO_2 + 2O_2 + 24H_2O$

(b) $0.65\ Ni(NO_3)_2.6H_2O + 0.40\ Zn(NO_3)_2.6H_2O + 1.95\ Fe(NO_3)_3.9H_2O + PEG \rightarrow Ni_{0.65}Zn_{0.40}Fe_{1.95}O_4 + 7.95NO_2 + 1.975O_2 + 23.85H_2O$

(c) $0.60\ Ni(NO_3)_2.6H_2O + 0.35\ Zn(NO_3)_2.6H_2O + 2.05\ Fe(NO_3)_3.9H_2O + PEG \rightarrow Ni_{0.60}Zn_{0.35}Fe_{2.05}O_4 + 8.05NO_2 + 2.025O_2 + 24.15H_2O$

The drying resulted in a reddish gel along with reddish brown fumes of NO_2 [26] which further converted into fluffy ferrite mass. The water content was removed with the use of a hot air oven for 10 hours. Each ferrite composition's as-prepared powder has been annealed at 400 ℃ for one hour and then allowed to cool naturally by turning off the furnace. The annealed powder was extensively crushed and made into pellets and toroids using polyvinyl alcohol as a binder. All the pellets and toroids have been heated for one hour at optimum temperatures (800 ℃ to 1050 ℃ @ 5℃/min) before being subjected to natural cooling to room temperature. The samples were further designated as IE-1000, IN-1050, and ID-1000, where 1000 and 1050 indicate the optimum annealing temperatures.

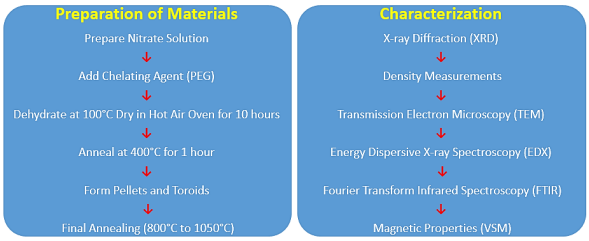

Flowchart 1: Preparation and characterization of Ni-Zn Ferrites

The preparation and characterization of Ni-Zn Ferrites are shown in flowchart 1 which ensuring clarity and reproducibility for future researchers.

Characterization

The samples have been characterized PANalytical X'Pert PRO was used for determining the crystallographic structure. SUPRA 55 Zeiss FESEM with attached EDX and working with a primary e-beam at an energy of 25 keV was used for morphological study. Nicolet-MAGNA-550 IR spectrometer was used for the compositional study. Detailed analysis and discussion about the observed variations in various parameters like lattice constant, and particle size, have been described as a function of iron content to finalize a composition with the desired characteristics of the magnetic hyperthermia application.

2.1 Materials

All the chemicals (Sulphuric acid, Buffer tablets, Potassium dichromate, 1,5-diphenyl carbazide, Nitric acid, Sodium hydroxide, etc) of analytical grade were purchased from Thermo Fisher Scientific India. 1000ppm stock solution of potassium dichromate, 0.1 N nitric acid, 5N sulphuric acid, 2N nitric acid, 0.1M & 2N sodium hydroxide, 0.25% DCPI solution and buffer solutions (pH-4.0,7.0 & 9.2) were prepared in different volumes.

3 Results and Discussion

3.1 XRD study

The spinel structure was tested and the lattice parameter of samples was been computed from the observed Bragg angles of the XRD in the range 15°–85° with 1.5406 Å wavelength X-rays. The XRD patterns of the samples IN, ID, and IE, Ni-Zn nanoferrite from 800 ℃ to 1050 ℃ are shown in Figures 1 to 3.

The wider peaks indicate the smaller crystallite size. The signs of nascent iron oxides are observed in the material. The intensity is increasing slowly with temperature indicating the enhancement of the crystallization. The estimated lattice parameters corresponding to the IN-1050, ID-1000, and IE-1000 samples were 8.3746 Å, 8.3774 Å, and 8.3806 Å respectively depending on the iron content from 50% to 51.25%. The marginal increase in the case of IE-1000 has been associated with the formation of Fe2+ ions in the material processed at a higher annealing temperature and the larger ionic radius of Fe2+ ions (0.78 Å).

The peaks (111), (220), (311), (222), (400), (422), (511), (440), (620), (533), (622) corresponds to JCPDS- 08-0234 and are cubic spinel structure. There is one extra peak in all three samples (IN 800℃; IE 800℃, and ID 900℃; 800℃, 900℃ and 1000℃) around 2= 40.9° is related to the iron oxide (Fe2O3) and is related to JCPDS 89-8104). The formation of the additional peak is due to the diffusion of atoms in the heating process [10, 27].

3.2 FESEM study

At the nanoscale, the size of particles becomes crucial due to the significant variations in material properties compared to larger micron-sized counterparts. Nano-sized ferrite particles, as they approach a critical diameter, display distinctive magnetic characteristics such as single domain behavior, superparamagnetism, and a lowered Curie temperature. Moreover, in nanoparticles with a high surface-to-volume ratio, surface spin disorder can alter magnetic properties over time. In single-domain particles, the absence of domain wall res-

onance shifts the operational frequency to higher ranges, making them valuable for high-frequency applications. Conversely, single-domain particles of sufficiently small size may demonstrate superparamagnetism, a property crucial for applications like magnetic hyperthermia treatment.

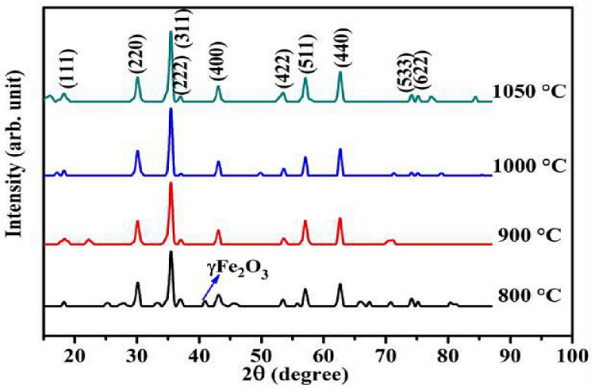

(a)

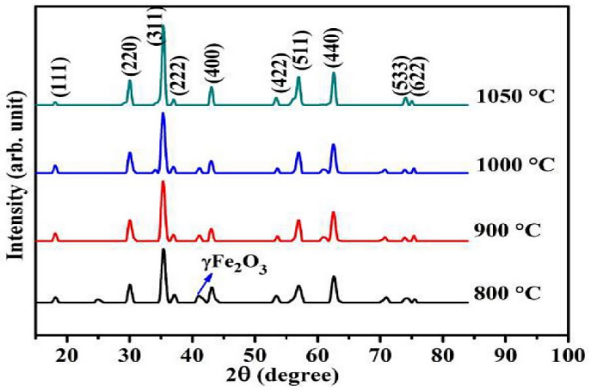

(b)

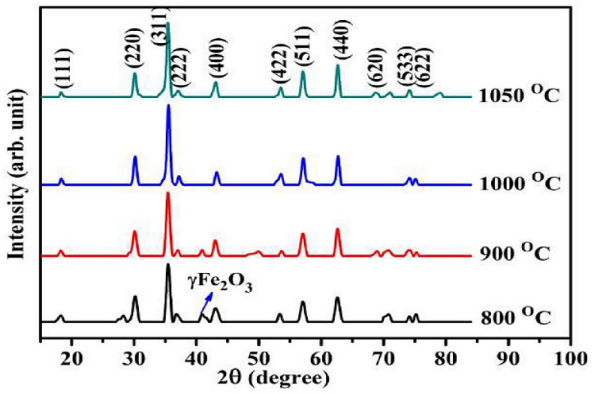

(c).

Figure 1: XRD of the (a) IN sample (b) ID sample and (c) IE sample subjected to various heating temperatures.

FESEM micrographs of these three samples support the observed microstructural changes in terms of increased porosity and compaction of reduced grains (Figure 2).

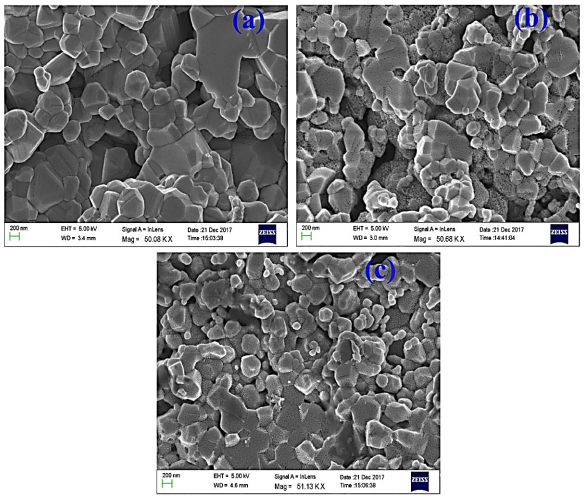

Figure 2: FESEM images of (a) IN-1050 (b) ID-1000 and (c) IE-1000 pellet samples.

Archimedes' principle has been used to determine the experimental (or) bulk density of all the samples.

The bulk density of the sample,

$$d_{bulk} = \frac{w_1}{w_1 - w_2} \tag{1}$$

where W_1 = the sample weight in air (g) W_2 = the sample weight in water (g)

The X-ray density is often more than the macroscopic density of a specimen which is influenced by the weight and volume of the specimen. This is because the macroscopic specimen, in contrast, exhibits minute cracks and pores. Determining the X-ray density, also known as "theoretical density", is essential because it may be used to evaluate actual porosity by comparing it to the macroscopic density of the sintered compacts. The theoretical density or X-ray density (dx-ray) has been calculated from the lattice parameter values using the expression below [28],

$$d_{X-ray} = \frac{8M}{Na^3} \tag{2}$$

where, M is the molecular weight of the ferrite sample, N is the Avogadro number and a is the lattice parameter of the unit cell.

From the values of X-ray and experimental densities, the percentage of porosity of the samples was calculated using the relation,

The percentage of porosity,

$$\frac{d_{X-ray} - d_{bulk}}{d_{X-ray}} \times 100 \tag{3}$$

The experimental density, X-ray density, and porosity of the samples have been presented in Table 1.

Table 1: Optimum firing temperatures, bulk density, X-ray density, and percentage of porosity of IN-1050, ID-1000, and IE-1000 samples

Composition	Optimum firing temperature (°C)	Bulk density (g/cm^3)	X-ray density (g/cm^3)	Porosity (%)
$Ni_{0.65}Zn_{0.35}Fe_{2.05}O_4$	1050	4.498	5.355	16.0
$Ni_{0.65}Zn_{0.40}Fe_{1.95}O_4$	1000	4.516	5.360	15.8
$Ni_{0.60}Zn_{0.35}Fe_{2.05}O_4$	1000	4.577	5.340	14.3

It is speculated that the production of Fe2+ ions in the sample processed at greater annealing temperatures is the cause of the higher bulk density of the IE-1000 composition. The larger sintering temperatures facilitate the reduction of Fe3+ ions into Fe2+ ions creating oxygen vacancies in the material which promotes the formation of larger grains with higher densities [27].

3.3 EDX spectra

Energy-dispersive X-ray spectroscopy (EDX) is used to record the elemental composition of the sintered samples. Figures 3 to 5 illustrate EDX spectra for the ID-1000, IE-1000, and IN-1050 samples. The observed presence of the elements, nickel (Ni), zinc (Zn), iron (Fe), and oxygen (O) in the spectra confirms that the nanoparticles belong to Ni-Zn ferrite material with no impurities.

3.4 FTIR spectra

Figure 6 represents the room temperature FTIR spectra recorded in the range from 3000 cm-1 to 300 cm-1 on the Nicolet-MAGNA-550 spectrometer using the KBr pellet for IN-1050, IE-1000, and ID-1000 samples.

Each spectrum has two significant absorption bands corresponding to Fe^{2+} O^{2-} vibrations at tetrahedral and octahedral sites, respectively, between 592-595 cm^{-1} and 414-420 cm^{-1} [29]. The absorption band 2363 cm^{-1} corresponds to the atmospheric carbon dioxide absorbed on the surface of the particles during sample preparation [30]. A weak band was observed at around 470 cm^{-1}, attributed to the splitting of the octahedral band due to the Jahn-Teller distortion, confirming the presence of the Fe^{2+}- O^{2-} vibration band in the ferrite [31]. Table 2 shows the band positions that correspond to tetrahedral and octahedral metal complexes.

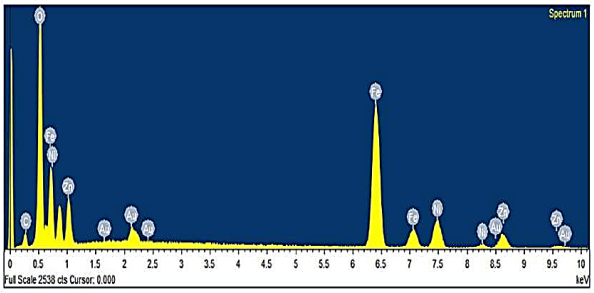

Figure 3: EDX spectra of ID-1000 sample.

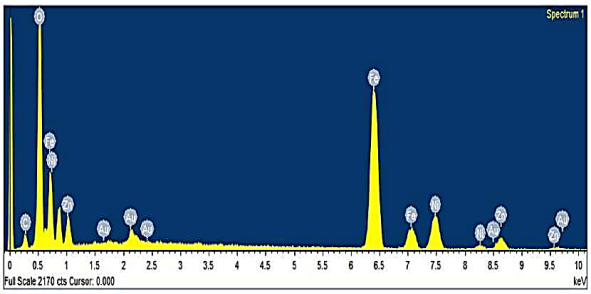

Figure 4: EDX spectra of IE-1000 sample.

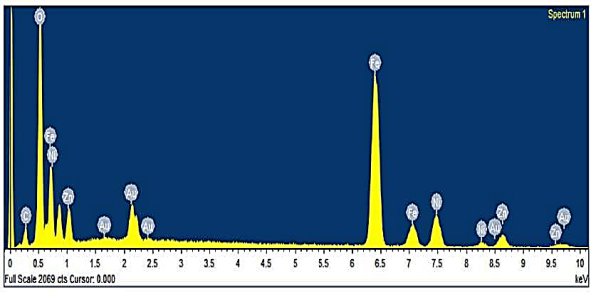

Figure 5: EDX spectra of IN-1050 sample.

Table 2: Band positions and Fe^{3+} - O^{2-} bond force constants for the samples.

Sample	(Tetrahedral) cm^{-1}	(Octahedral) cm^{-1}	Fe^{3+}-O^{2-} Bond force constant (10^5 dyne/cm)	
			Tetrahedral (Kt)	Octahedral (Ko)
IN 1050	592	414	227	133
ID 1000	595	417	223	135
IE 1000	593	420	228	137

In comparison to the corresponding bands of IN-1050, the tetrahedral band ($v1$) of ID-1000 and octahedral band ($v2$) of IE-1000 exhibit a shift towards the higher wave numbers. The tetrahedral band shift suggests that Zn^{2+} (0.60 Å) ions prefer to occupy tetrahedral sites and push Fe^{3+} ions towards oxygen ions due to the larger ionic radius of Zn^{2+} than Fe^{3+} (0.49 Å) ion. This is expected to result in a decrease in the distance between Fe^{3+} - O^{2-} ions. The presence of a weak absorption band, 668 cm^{-1} could be attributed to the presence of the Zn^{2+} ions at the tetrahedral sites [32] corresponding to the Zn^{2+} - O^{2-} tetrahedral complexes. An increase in zinc concentration resulted in a corresponding increase in band intensity (Figure 7) in the ID-1000 sample.

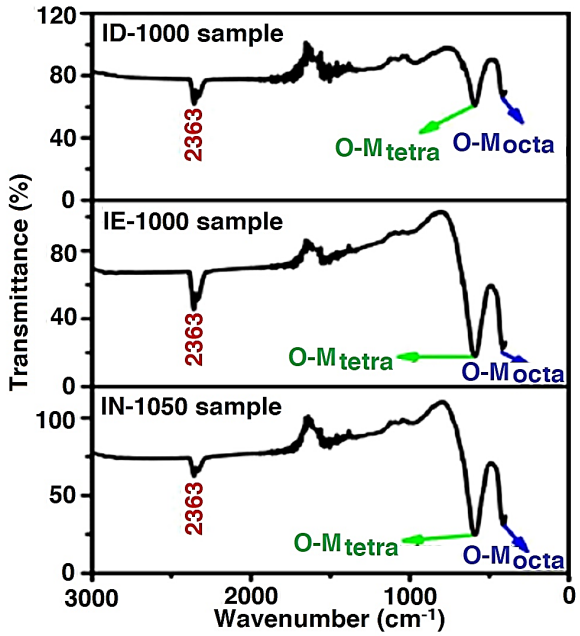

Figure 6: FTIR spectra of Ni-Zn ferrites.

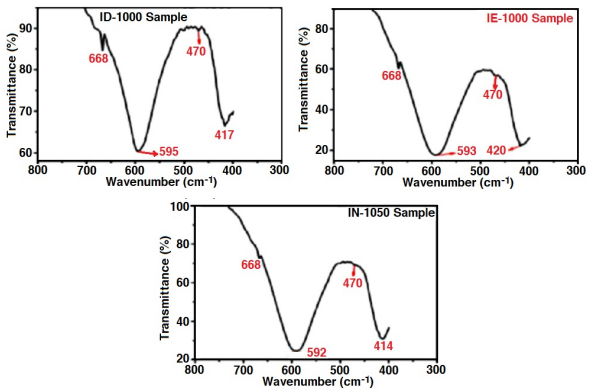

Figure 7: Magnified pictures of absorption bands of Ni-Zn ferrite samples.

Due to a change in bond length at B-sites, there is a shift of the octahedral absorption band in the IE-1000 sample causing an increase in the force constant of the octahedral site when compared to the normal sample. The force constant for the Fe^{3+} - O^{2-} bond has been estimated with the help of the formula shown below [33],

$$K = 4^2 c^{22} \tag{4}$$

(all values are in CGS), where c is the speed of light, is the wave number and is the reduced mass for Fe3+ and O2- ions. **Table 2** shows the estimated force constants for the tetrahedral and octahedral sites. Generally, there is a decrease in bond length and an increase in force constant for either site if the radius of the impurity ion is lower than the displaced ion. The concentration of displaced nickel ion and the excess iron ion is the same in the IE-1000 sample. The rise in iron concentration at octahedral sites could improve the reduced mass, besides substituting the nickel ions at octahedral sites and the process is in charge of the variations noticed in band position and force constant.

To have the quantitative distribution of ions on tetrahedral and octahedral sites, effective cation distribution is needed. Further, the distribution helps to discuss the changes taking place in the peak position of the absorption bands with the amount of iron content in the Ni-Zn system. For this purpose, the cation distribution has been proposed based on experimentally obtained saturation magnetization measurements.

4 Conclusions

The sol-gel process was adopted in preparing the Ni-Zn nanoferrites with varying amounts of iron in the composition. XRD shows cubic spinel structure except for one extra peak in all three samples (IN 800℃; IE 800℃, and ID 900℃; 800℃, 900℃ and 1000℃) around 2= 40.9° is related to the iron oxide (Fe2O3) and is related to JCPDS 89-8104). In comparison to the IN-1050 bands, the ID-1000 and IE-1000 samples exhibit shifts towards higher wave numbers in the tetrahedral and octahedral bands, respectively. A weak band was observed at around 470 cm^{-1} in FTIR spectroscopy, attributed to the splitting of the octahedral band due to the Jahn-Teller distortion, confirming the presence of the Fe^{2+}- O^{2-} vibration band in the ferrite. There is a decrease in bond length and an increase in force constant for either site if the radius of the impurity ion is lower than the displaced ion. The iron content explicitly affect the magnetic and hence hyperthermial phenomena.

References

[1] P. Gas. Essential facts on the history of hyperthermia and their connections with electromedicine. *Przeglad Elektrotechniczny*, 87(12B):37–40, 2011.

[2] H. Fatima, T. Charinpanitkul, and K. S. Kim. Fundamentals to apply magnetic nanoparticles for hyperthermia therapy. *Nanomaterials*, 11(5), 2021.

[3] D. Parajuli, N. Murali, and K. Samatha. Correlation between the magnetic and dc resistivity studies of cu substituted ni and zn in ni-zn ferrites. *BIBECHANA*, 19(1–2):61–67, Sep 2022.

[4] D. Parajuli, P. Taddesse, N. Murali, and K. Samatha. Study of structural, electromagnetic and dielectric properties of cadmium substituted ni–zn nanosized ferrites. *Journal of the Indian Chemical Society*, 99(3):100380, Mar 2022.

[5] D. Parajuli and K. Samatha. Structural analysis of cu substituted ni\zn in ni-zn ferrite. *BIBECHANA*, 18(1):128–133, Jan 2021.

[6] D. Parajuli and K. Samatha. Morphological analysis of cu substituted ni\zn in ni-zn ferrites. *BIBECHANA*, 18(2):80–86, May 2021.

[7] A. M. Kumar, M. C. Varma, C. L. Dube, K. H. Rao, and S. C. Kashyap. Development of ni–zn nanoferrite core material with improved saturation magnetization and dc resistivity. *Journal of Magnetism and Magnetic Materials*, 320(14):1995–2000, Jul 2008.

[8] A. Verma, T. C. Goel, R. G. Mendiratta, and M. I. Alam. Dielectric properties of nizn ferrites prepared by the citrate precursor method. *Materials Science and Engineering: B*, 60(2):156–162, Jun 1999.

[9] X. Jia, D. Chen, X. Jiao, T. He, and H. Wang. Monodispersed co, ni-ferrite nanoparticles with tunable sizes: controlled synthesis, magnetic properties, and surface modification. *Journal of Physical Chemistry C*, 2008. Accessed: Nov. 07, 2023.

[10] R. M. Mohamed, M. M. Rashad, F. A. Haraz, and W. Sigmund. Structure and magnetic properties of nanocrystalline cobalt ferrite powders synthesized using organic acid precursor method. *Journal of Magnetism and Magnetic Materials*, 322(14):2058–2064, Jul 2010.

[11] M. Atif, M. W. Asghar, M. Nadeem, W. Khalid, Z. Ali, and S. Badshah. Synthesis and investigation of structural, magnetic and dielectric properties of zinc substituted cobalt ferrites. *Journal of Physics and Chemistry of Solids*, 123:36–42, Dec 2018.

[12] A. V. Raut, R. S. Barkule, D. R. Shengule, and K. M. Jadhav. Synthesis, structural investigation and magnetic properties of zn2+ substituted cobalt ferrite nanoparticles prepared by the sol–gel auto-combustion technique. *Journal of Magnetism and Magnetic Materials*, 358–359:87–92, May 2014.

[13] T. Zeeshan, S. Anjum, S. Waseem, and L. Mustufa. Tailoring of structural and magnetic properties by substitution of copper in cobalt chromium ferrites. *Ceramics International*, 44(15):17709–17715, Oct 2018.

[14] G. Kumar et al. Superparamagnetic behaviour and evidence of weakening in super-exchange interactions with the substitution of gd3+ ions in the mg–mn nanoferrite matrix. *Materials Research Bulletin*, 63:216–225, Mar 2015.

[15] P. Appa Rao et al. A systematic study of cobalt-zinc ferrite nanoparticles for self-regulated magnetic hyperthermia. *Journal of Alloys and Compounds*, 794:60–67, Jul 2019.

[16] T. J. Shinde, A. B. Gadkari, and P. N. Vasambekar. Magnetic properties and cation distribution study of nanocrystalline ni–zn ferrites. *Journal of Magnetism and Magnetic Materials*, 333:152–155, May 2013.

[17] H. Kavas, A. Baykal, M. S. Toprak, Y. Köseoğlu, M. Sertkol, and B. Aktaş. Cation distribution and magnetic properties of zn doped nife2o4 nanoparticles synthesized by peg-assisted hydrothermal route. *Journal of Alloys and Compounds*, 479(1–2):49–55, Jun 2009.

[18] P. Gao et al. Structural and magnetic properties of ni1xznxfe2o4 (x=0, 0.5 and 1) nanopowders prepared by sol–gel method. *Journal of Magnetism and Magnetic Materials*, 348:44–50, Dec 2013.

[19] H. Su, H. Zhang, X. Tang, Y. Jing, and Y. Liu. Effects of composition and sintering temperature on properties of nizn and nicuzn ferrites. *Journal of Magnetism and Magnetic Materials*, 310(1):17–21, Mar. 2007.

[20] K. Sun, Z. Lan, Z. Yu, X. Jiang, and J. Huang. Phase formation, grain growth and magnetic properties of nicuzn ferrites. *Journal of Magnetism and Magnetic Materials*, 323(7):927–932, Apr. 2011.

[21] X. He, G. Song, and J. Zhu. Non-stoichiometric nizn ferrite by sol-gel processing. *Materials Letters*, 59(14–15):1941–1944, Jun. 2005.

[22] D. Parajuli, S. Uppugalla, N. Murali, A. Ramakrishna, B. Suryanarayana, and K. Samatha. Synthesis and characterization mxene-ferrite nanocomposites and its application for dying and shielding. *Inorganic Chemistry Communications*, 148:110319, Feb. 2023.

[23] D. Parajuli and K. Samatha. Structural and cation distribution analysis of nickel-copper/nickel-magnesium substituted lithium ferrites. *BIBECHANA*, 21(1):74–82, Mar. 2024.

[24] D. Parajuli, N. Murali, and K. Samatha. Cr3+ substitution effect on co-cu and cu-co nano ferrites on structural and morphological properties. *BIBECHANA*, 20(3):275–284, Nov. 2023.

[25] D. D. Andhare, S. R. Patade, M. V. Khedkar, A. A. Nawpute, and K. M. Jadhav. Intensive analysis of uncoated and surface modified co-zn nanoferrite as a heat generator in magnetic fluid hyperthermia applications. *Applied Physics A: Materials Science and Processing*, 128(6), Jun. 2022.

[26] J. S. Ghodake, R. C. Kambale, T. J. Shinde, P. K. Maskar, and S. S. Suryavanshi. Magnetic and microwave absorbing properties of co2+ substituted nickel–zinc ferrites with the emphasis on initial permeability studies. *Journal of Magnetism and Magnetic Materials*, 401:938–942, Mar. 2016.

[27] C. Sujatha, K. V. Reddy, K. S. Babu, A. R. Reddy, and K. H. Rao. Effects of heat treatment conditions on the structural and magnetic properties of mgcuzn nano ferrite. *Ceramics International*, 38(7):5813–5820, Sep. 2012.

[28] S. B. Singh et al. Structural, thermal and magnetic studies of mgxzn1xfe2o4 nanoferrites: Study of exchange interactions on magnetic anisotropy. *Ceramics International*, 42(16):19179–19186, Dec. 2016.

[29] M. M. Mallapur, P. A. Shaikh, R. C. Kambale, H. V. Jamadar, P. U. Mahamuni, and B. K. Chougule. Structural and electrical properties of nanocrystalline cobalt substituted nickel zinc ferrite. *Journal of Alloys and Compounds*, 479(1–2):797–802, Jun. 2009.

[30] M. Sangmanee and S. Maensiri. Nanostructures and magnetic properties of cobalt ferrite (cofe 2o4) fabricated by electrospinning. *Applied Physics A: Materials Science and Processing*, 97(1):167–177, Oct. 2009.

[31] N. Singh, A. Agarwal, S. Sanghi, and P. Singh. Effect of magnesium substitution on dielectric and magnetic properties of ni–zn ferrite. *Physica B: Condensed Matter*, 406(3):687–692, Feb. 2011.

[32] A. Pradeep and G. Chandrasekaran. Ftir study of ni, cu and zn substituted nano-particles of mgfe2o4. *Materials Letters*, 60(3):371–374, Feb. 2006.

[33] P. A. Shaikh, R. C. Kambale, A. V. Rao, and Y. D. Kolekar. Structural, magnetic and electrical properties of co–ni–mn ferrites synthesized by co-precipitation method. *Journal of Alloys and Compounds*, 492(1–2):590–596, Mar. 2010.